Electromagnetic Science
vol. 1, no. 3, 0030062, September 2023
https://doi.org/10.23919/emsci.2023.0006

Research Article

Electromagnetic Technology for Vacuum Metrology in the Typical Development of a Metrological-Grade Spinning Rotor Gauge

Detian Li, Meiru Guo, Zhenhua Xi, Huzhong Zhang, and Bowen Li

Science and Technology on Vacuum Technology and Physics Laboratory, Lanzhou Institute of Physics, Lanzhou 730000, China

Corresponding author: Detian Li, Email: lidetian@hotmail.com.
Received February 22, 2023; Accepted August 7, 2023; Published Online August 17, 2023.

Abstract — As the most precise viscous vacuum gauge, the spinning rotor gauge is widely used in the aerospace, nuclear, semiconductor, and other fields because of its excellent accuracy and chemical inertness. Herein, a metrological-grade spinning rotor vacuum gauge is developed, and its performance is evaluated. It can be used for international comparison of vacuum standards and construction of national vacuum measurement traceability and transmission systems. This paper presents the design of a single-degree-of-freedom permanent magnet-biased rotor suspension system, a high-speed rotary stepper drive system, a rotational angular velocity determination system, a lateral damping system, and a transducer in detail. The change in residual drag is less than 0.49% after 50 minutes of start-up. There is good consistency and linearity in the range of 9.1727×10^{-5} Pa to 1.2081 Pa.

Keywords — Magnetically levitated rotor, Vacuum metrology, Transfer standard, Viscous vacuum gauge.

Citation — Detian Li, Meiru Guo, Zhenhua Xi, *et al.*, "Electromagnetic Technology for Vacuum Metrology in the Typical Development of a Metrological-Grade Spinning Rotor Gauge," *Electromagnetic Science*, vol. 1, no. 3, article no. 0030062, 2023. doi: 10.23919/emsci.2023.0006.

I. Introduction

Electromagnetic technology has an extensive range of applications in vacuum metrology. In particular, various vacuum measuring instruments based on the electromagnetic principle have been developed for accurate and indirect measurement of specific physical quantities that are proportional to the total pressure or partial pressure in vacuum [1]–[3], for example, spinning rotor gauges (SRGs), inverted magnetron cold cathode ionization gauges (IMGs), time-of-flight mass spectrometers (TOF MSs), and magnetic sector mass spectrometers.

As an emerging technology in the 20th century, magnetic levitation technology can avoid friction and abrasion between objects, prolong the equipment life and improve the equipment operating conditions due to its contactless characteristics [4]. Owing to the application of magnetic levitation technology, the additional pressure-independent frictional drag is significantly reduced, so higher accuracy and stability can be achieved by an SRG [5]–[12]. An SRG has typically become the most accurate vacuum gauge in the high vacuum range [13]–[18]. It is widely used in the aerospace, nuclear, semiconductor, and other fields because of its excellent accuracy and chemical inertness [1], [2]. The mechanism of residual drag generation has long been the focus of SRG research, which mainly includes the eddy current effect, relaxation effect, and Coriolis effect [19]–[22]. In the 1980s, Cong *et al.* carried out the development of the prototype of CXG-1 [23].

In this study, the development of a state-of-the-art metrological-grade SRG is introduced. The relevant parameters are obtained through theoretical calculations and numerical simulations, and the structure of each subsystem is designed. Finally, its metrological characteristics are presented.

II. Principle

The measuring principle of an SRG is based on the frictional force between gaseous molecules and a magnetically suspended rotor in vacuum. The gas molecules hit the rotor surface, remain there for some time and then leave the surface with the additional tangential velocity of the rotor surface. This additional momentum of the gas molecule is gained from the momentum of the rotor, thereby reducing its rotational angular velocity [1]–[3].

For a spherical rotor as shown in Figure 1, accordingly, the pressure can be written as [18]

$$p = \frac{\pi \bar{c} \rho d}{20\sigma}\left(-\frac{\dot{\omega}}{\omega} - \alpha_{\mathrm{RD}}\right) \quad (1)$$

where $\bar{c}$ is the average thermal velocity of the gas, ρ is the density of the spherical rotor, d is the diameter of the spherical rotor, σ is the accommodation factor, ω is the rotational angular velocity, and a_{RD} is the pressure-independent residual drag.

III. Structure and Design

A schematic diagram of the SRG is shown in Figure 2. It includes a single-degree-of-freedom permanent magnet-biased rotor suspension system, a high-speed rotary stepper drive system, a rotational angular velocity determination system, a lateral damping system, and a transducer. During determination, the spherical rotor is magnetically levitated by the suspension system and accelerated to a particular working rotational speed (400–500 Hz) by the drive system.

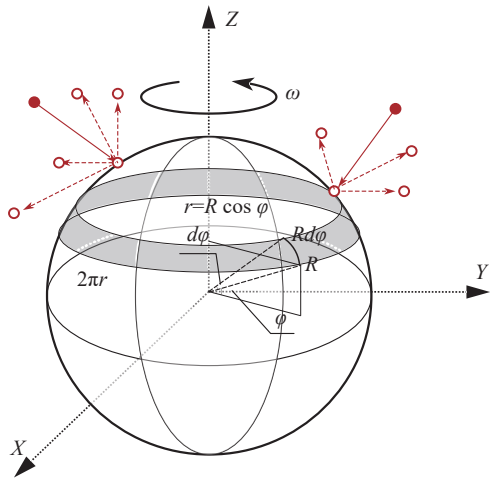

Figure 1 Schematic diagram of the friction between gas molecules and the rotor.

Then, the rotor maintains coasting with a gradual decaying velocity measured by the determination system. The subsystems are described as follows.

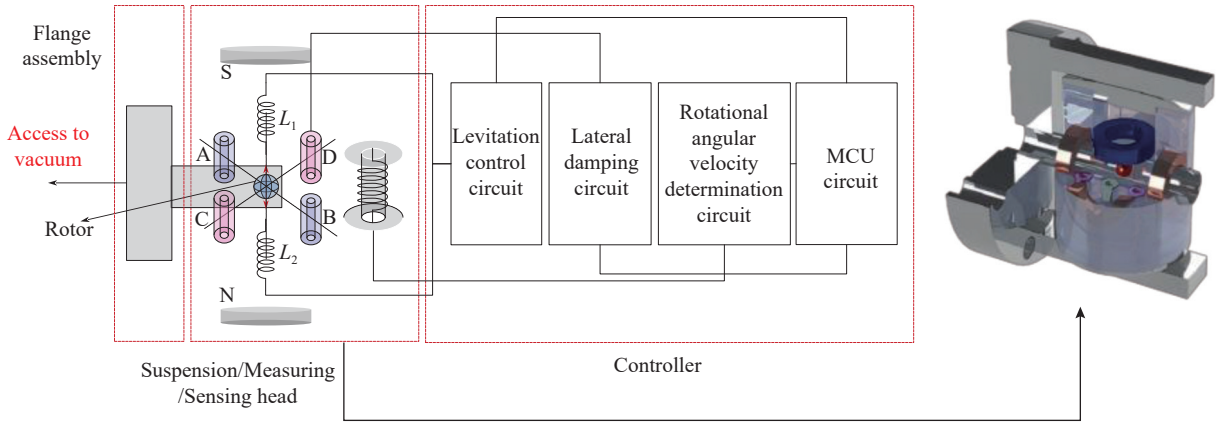

Figure 2 Schematic diagram of the SRG (the legend of the picture on the far right: rotor (red); suspension coils (blue); rotary driving coils (bronze); lateral damping coils (purple); pickup coils (green); and vacuum thimble (silver)).

1. Single-degree-of-freedom permanent magnet-biased rotor suspension system

1) PM-EM hybrid magnetic levitation model

As mentioned above, magnetic levitation is a prerequisite for determination. From Earnshaw's theorem, it is impossible to achieve static, stable magnetic levitation by permanent magnets alone. Therefore, a hybrid permanent magnet (PM)-biased and electromagnetic (EM) excitation structure as shown in Figure 3 is used to achieve stable levitation of the spherical rotor. The PM provides most of the magnetic field required for rotor levitation. The EM coils generate an electromagnetic field for regulation and control to ensure stable levitation. With the same excitation capacity, the number of turns of the solenoid coil can be reduced to diminish the system inductance, improve the system response speed, enhance the system stability, reduce the system power consumption, and thus reduce the influence of temperature on the measurement. The suspension coils are eddy current displacement sensors driven by a high-frequency AC excitation. When the rotor deviates from the equilibrium position, the common end of the two coils produces phase and amplitude changes relative to the excitation signal. Two signals from the AC bridge are introduced into the phase-sensitive detector circuit. Through conditioning, the circuit produces a DC signal, and this signal, as the error signal of the rotor axial displacement, is passed into a proportional-integral-derivative (PID) feedback controller. The suspension coils also act as the actuators of suspension control, thus forming an effective closed-loop control system.

The levitation system must be accurately modeled, considering all factors affecting the axial levitation system. For the convenience of the study, the following assumptions are made without affecting the modeling and experiments:

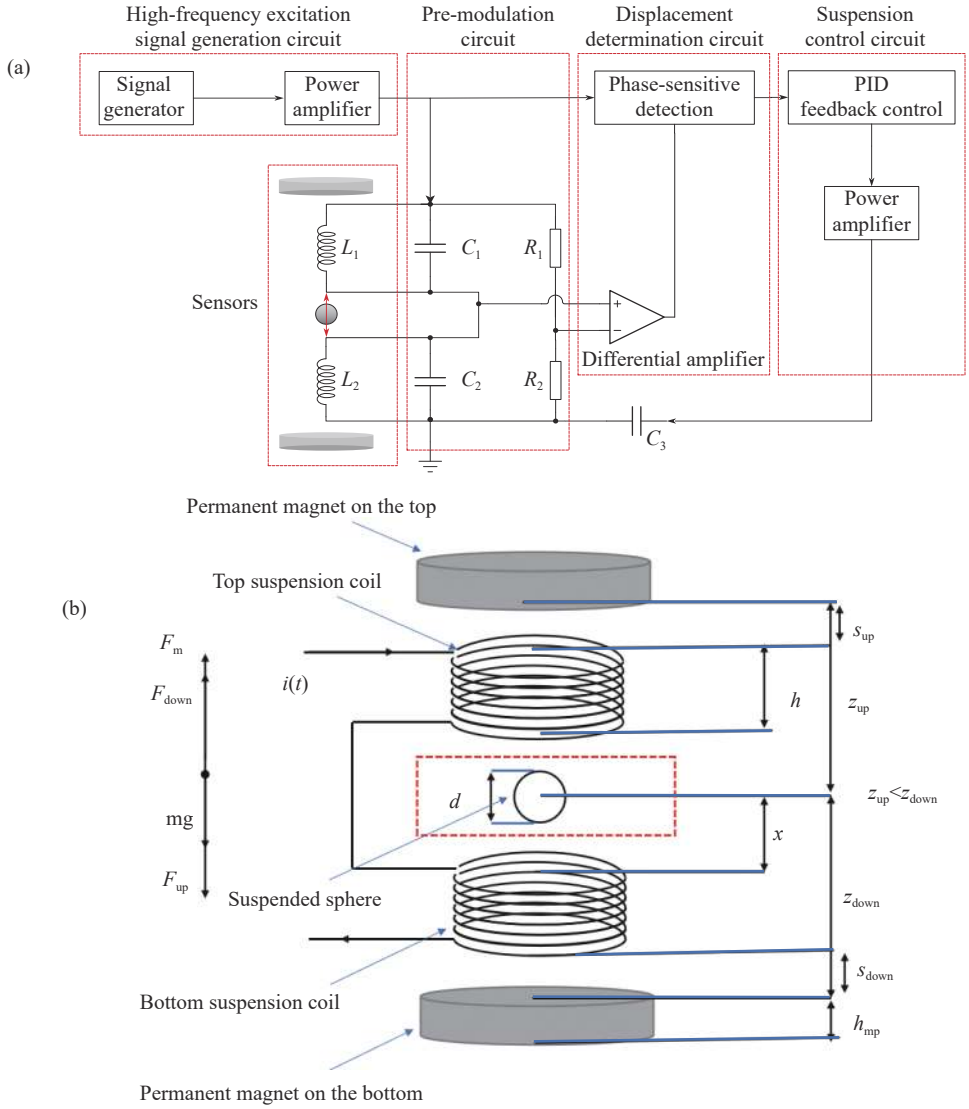

Figure 3 (a) Schematic diagram of the PM-EM hybrid magnetic levitation system; (b) Enlargement of the sensor section of subfigure (a), in which s_{up} represents the length of the air gap between the upper permanent magnet and the upper coil; s_{down}, the length of the air gap between the lower permanent magnet and the lower coil; h_{mp}, the thickness of the permanent magnet; h, the thickness of the coil; z_{up}, the distance from the sphere to the upper permanent magnet; z_{down}, the distance from the sphere to the lower permanent magnet; x, the distance from the sphere to the plane of the lower coil; d, the diameter of the sphere; $i(t)$, the coil current; F_m, the magnetic force between the upper and lower permanent magnets at the equilibrium point; $F_{up}(x,i)$, the upper coil attraction; $F_{down}(x,i)$, the lower coil attraction; m, the spherical sphere mass; g, the acceleration of gravity.

i) The magnetization of the permanent magnet is uniform, and there is no decay of the magnetic potential of the axial magnetic field with time or temperature.

ii) The magnetic permeability of the ferromagnetic materials (i.e., metallic sphere and permanent magnet) is infinite.

iii) The leakage between the coil and the permanent magnet in the air gap can be ignored.

iv) The thimble, coil, and permanent magnet have infinite stiffness and do not undergo any elastic deformation.

v) The action of the measuring gas on the spherical rotor can be neglected.

vi) The effect of the flange thimble on the electromagnetic field can be ignored.

The red box in Figure 3(b) shows the metal thimble connected to the vacuum system, which restricts the spherical rotor motion. The kinetic equation for the spherical rotor levitation can be expressed by

$$m\frac{\mathrm{d}^2x(t)}{\mathrm{d}t^2} = -F_{up}(x,i) + F_{down}(x,i) - F_m + mg \qquad (2)$$

where m is the mass of the spherical rotor.

First, the magnetic flux density of the permanent magnet at the center axis is analyzed, and its model is established, as shown in Figure 4.

By assumption i), the permanent magnet is uniformly magnetized. The magnetization $\boldsymbol{M}$ is a constant vector, so the volume current density is zero. By Ampere's circuital law, the cylindrical permanent magnet can be equated to a cylindrical circulation flowing along the tangential direction of the cylindrical side with current magnitude M and

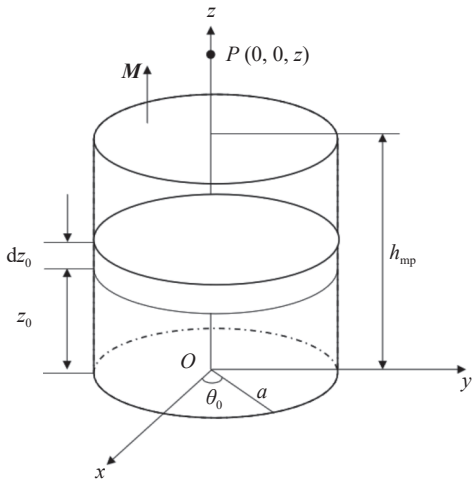

Figure 4 Model of the axial magnetic flux density of the cylindrical permanent magnet.

no current on the top and bottom surfaces. Taking the differential length of the cylindrical surface (see Figure 3) as dz_0, the distance of the cylindrical surface from the bottom surface as z_0, the angle at which the circulating current passes through as θ_0, and the surface current flowing on dz_0 as $M dz_0 \theta$, the dB_m generated by this surface current at point P is

$$dB_m = \frac{\mu_0 M a^2 dz_0}{2\left[(z-z_0)^2 + a^2\right]^{3/2}} \hat{z} \tag{3}$$

By integrating along the height of the cylinder, the magnetic flux density B_m generated by the cylindrical permanent magnet at point P on the central axis can be obtained as

$$B_m = \int_0^{h_{mp}} dB_m = \frac{\mu_0 M}{2}\left[\frac{z}{\sqrt{z^2+a^2}} - \frac{z-h_{mp}}{\sqrt{(z-h_{mp})^2+a^2}}\right]\hat{z} \tag{4}$$

That is,

$$\begin{cases} B_x = 0, \quad B_y = 0 \\ B_z = \dfrac{\mu_0 M}{2}\left(\dfrac{z}{\sqrt{z^2+a^2}} - \dfrac{z-h}{\sqrt{(z-h)^2+a^2}}\right) \end{cases} \tag{5}$$

where μ_0 is the magnetic permeability of free space.

From equation (4), it can be seen that if the two permanent magnets are perfectly symmetrical about the central point, then the magnetic flux densities generated by the permanent magnets on opposite sides will cancel each other out and cannot play the role of balancing part of the gravity of the small sphere. This problem is also considered in the actual design, so the upper and lower permanent magnets are arranged asymmetrically, as shown in Figure 4.

Based on the above derivation, the equations for the permanent magnet force versus magnetic flux density in the direction of the central axis are summarized as

$$\begin{cases} F_m = \dfrac{\left(B_{mup}^2 - B_{mdown}^2\right)S}{2\mu_0} \\ B_{mup} = \frac{\mu_0 M}{2}\left(\dfrac{z_{up}}{\sqrt{z_{up}^2+a^2}} - \dfrac{z_{up}-h_{mp}}{\sqrt{(z_{up}-h_{mp})^2+a^2}}\right) \\ B_{mdown} = \dfrac{\mu_0 M}{2}\left(\dfrac{z_{down}}{\sqrt{z_{down}^2+a^2}} - \dfrac{z_{down}-h_{mp}}{\sqrt{(z_{down}-h_{mp})^2+a^2}}\right) \\ z_{up} = s_{up} + (0.01 - x) \\ z_{down} = s_{down} + x \end{cases} \tag{6}$$

where B_{mup} is the magnetic flux density generated by the lower permanent magnet at the radial plane of the rotor, B_{mdown} comes from the upper magnet, and S is the cross-sectional area of the spherical rotor.

With the above equations, the magnetic force of the permanent magnet on the rotor at a specific position in space can be obtained as

$$F_m(x) = \frac{\mu_0 M^2 S}{8}\left[\left(\frac{s_{up}+(0.01-x)}{\sqrt{[s_{up}+(0.01-x)]^2+a^2}} - \frac{s_{up}+(0.01-x)-h_{mp}}{\sqrt{(s_{up}+(0.01-x)-h_{mp})^2+a^2}}\right)^2 - \left(\frac{s_{down}+x}{\sqrt{(s_{down}+x)^2+a^2}} - \frac{s_{down}+x-h_{mp}}{\sqrt{(s_{down}+x-h_{mp})^2+a^2}}\right)^2\right] \tag{7}$$

From equation (7), it can be seen that the force of the permanent magnet on the rotor is only related to its axial position x. Therefore, once the axial levitation position x is determined by the design of the solenoid control loop, the permanent magnet force on the rotor is governed only by the mounting positions of the permanent magnets s_{down} and s_{up}. Thus, in the design of the hybrid magnetic levitation system, the mounting positions of the permanent magnets can be adjusted according to the rotor mass.

The electromagnetic force generated by the suspension coil is deduced from Kirchhoff's law and the Biot-Savart law and can be expressed as

$$F_{up}(x,i) = -\frac{\mu_0 S N^2}{2}\left(\frac{i}{x}\right)^2 \tag{8}$$

$$F_{down}(x,i) = \frac{\mu_0 S N^2}{2}\left(\frac{i}{0.01-x}\right)^2 \tag{9}$$

where N is the number of turns and 0.01 m is the distance between the upper and lower suspension coils, or 10 mm. To simplify the calculation, the following constant term is defined:

$$K = \frac{\mu_0 S N^2}{2} \tag{10}$$

From equation (2) to (10), the kinetic equation for the levitation of the rotor can be obtained as follows:

$$m\frac{\mathrm{d}^2x(t)}{\mathrm{d}t^2} = -K\left(\frac{i(t)}{x(t)}\right)^2 + K\left(\frac{i(t)}{0.01-x(t)}\right)^2 - F_{\mathrm{m}}(x) + mg \quad (11)$$

When working at the equilibrium point (i.e., the geometric center point between the two suspension coils, 5 mm from the lower coil), in the ideal case, the current in the suspension coils will be zero; otherwise, the mechanical equilibrium will be disrupted. However, this is not in accordance with the applicable working conditions. It is known that the magnetic force generated by a single permanent magnet cannot produce stable magnetic levitation, so a slight deviation is introduced as a correction, that is, x_0 = 0.0051 m is taken. The working current is i_0; to achieve as low as possible or even zero power control, here, the desired current is set as 0.01 A.

$$m\frac{\mathrm{d}^2x(t)}{\mathrm{d}t^2} = K_x \cdot x(t) + K_i \cdot i(t) \quad (12)$$

Here,

$$K_x = \frac{2i_0^2K}{(0.01-x_0)^3} + \frac{2i_0^2K}{x_0^3}$$

$$-\frac{1}{8}M^2\mu_0 S \times \left\{ \begin{array}{l} 2\times\left(\dfrac{s_{\mathrm{up}}-x_0+0.01}{\sqrt{a^2+(s_{\mathrm{up}}-x_0+0.01)^2}} - \dfrac{-h_{\mathrm{mp}}+s_{\mathrm{up}}-x_0+0.01}{\sqrt{a^2+(-h_{\mathrm{mp}}+s_{\mathrm{up}}-x_0+0.01)^2}}\right) \\ \times\left(-\dfrac{(-h_{\mathrm{mp}}+s_{\mathrm{up}}-x_0+0.01)^2}{\left(a^2+(-h_{\mathrm{mp}}+s_{\mathrm{up}}-x_0+0.01)^2\right)^{3/2}} + \dfrac{1}{\sqrt{a^2+(-h_{\mathrm{mp}}+s_{\mathrm{up}}-x_0+0.01)^2}}\right. \\ \left. +\dfrac{(s_{\mathrm{up}}-x+0.01)^2}{\left(a^2+(s_{\mathrm{up}}-x+0.01)^2\right)^{3/2}} - \dfrac{1}{\sqrt{a^2+(s_{\mathrm{up}}-x_0+0.01)^2}}\right) \\ -2\times\left(\dfrac{s_{\mathrm{down}}-x_0+0.01}{\sqrt{a^2+(s_{\mathrm{down}}-x_0+0.01)^2}} - \dfrac{s_{\mathrm{down}}-h_{\mathrm{mp}}-x+0.01}{\sqrt{a^2+(s_{\mathrm{down}}-h_{\mathrm{mp}}-x+0.01)^2}}\right) \\ \times\left(-\dfrac{(s_{\mathrm{down}}-h_{\mathrm{mp}}-x_0+0.01)^2}{\left(a^2+(s_{\mathrm{down}}-h_{\mathrm{mp}}-x_0+0.01)^2\right)^{3/2}} + \dfrac{1}{\sqrt{a^2+(s_{\mathrm{down}}-h_{\mathrm{mp}}-x_0+0.01)^2}}\right. \\ \left. +\dfrac{(s_{\mathrm{down}}-x_0+0.01)^2}{\left(a^2+(s_{\mathrm{down}}-x_0+0.01)^2\right)^{3/2}} - \dfrac{1}{\sqrt{a^2+(s_{\mathrm{down}}-x_0+0.01)^2}}\right) \end{array} \right\} \quad (13)$$

$$K_i = \frac{2i_0K}{(0.01-x_0)^2} - \frac{2i_0K}{x_0^2} \quad (14)$$

where K_x and K_i are the displacement stiffness coefficient and current stiffness coefficient, respectively. Applying the Laplace transform to equation (11), we obtain

$$mx(s)s^2 = K_x x(s) + K_i i(s) \quad (15)$$

Furthermore,

$$\frac{x(s)}{i(s)} = \frac{K_i}{ms^2 - K_x} \quad (16)$$

From equation (16), it can be seen that the frequency domain model of this system is extremely similar to that of the magnetic levitation system controlled only by electromagnetic action in that both the "current stiffness coefficient" and the "displacement stiffness coefficient" are used to characterize the effect of excitation current changes and displacement changes in the system. However, according to equation (12), it can be implied that the displacement stiffness coefficient derived in this paper contains variables related to parameters such as the magnetization strength, size, and mounting positions of the permanent magnets. The specific parameters used are listed in Table 1.

The transfer function of the hybrid magnetic levitation system is obtained by substituting the parameters in the table.

$$G(s) = -\frac{2.74638\times10^{-3}}{s^2 + 5398.42} \quad (17)$$

2) Finite element simulation analysis

By using ANSYS Maxwell analysis and substituting the materials and parameters determined in the previous section, the magnitude of the levitation force on the magnetically levitated spherical rotor can be visually obtained so that the correctness of the physical model can be verified by the magnetic flux density and the force.

Considering the complex structure of the SRG and the accuracy of the simulation, the assumptions and boundary conditions are set as follows: a) The end effect of the coil is not considered; b) The magnetic field is assumed to be uniformly distributed in the axial direction; c) The skin effect and proximity effect of the coil are not considered; and d) The boundary of the simulation model is set to be magnetically insulated, namely, the magnetic lines of force are parallel to the boundary.

In the grid independence and region independence

Table 1 Parameter table of the single-degree-of-freedom permanent magnet-biased rotor suspension system

Parameters	Value
Vacuum magnetic permeability μ_0 (H/m)	$4\pi\times10^{-7}$
NdFeB magnetization strength M (A/m)	1.032×10^{6}
Coil thickness h (mm)	3
Coil inner diameter r (mm)	5
Cross-sectional area of the rotor S ($m^{2)}$	1.59×10^{-5}
Number of turns of the coil N (turn)	400
Spherical rotor mass m (g)	0.3726
Gravitational acceleration g (m/s^2)	9.8
Upper permanent magnet air gap s_{up} (mm)	4.5
Lower permanent magnet air gap s_{up} (mm)	5
Thickness of cylindrical permanent magnets h_{hmp} (mm)	3
Radius of cylindrical permanent magnets a (mm)	10
Distance from the lower coil at balance x_0 (mm)	5.1
Coil current at balance i_0(mA)	10

Note: This model uses a hollow coil to realize the electromagnetic levitation part, and the rotor diameter is smaller than the inner diameter of the coil. The rotor can thus be considered to only be subject to the magnetic flux through its radial cross-section, so the rotor cross-sectional area S is used for the electromagnetic calculation.

analysis, the error is only 0.54% and 0.34% when the computational region radius is scaled from 40 mm to 50 mm and from 35 mm to 40 mm, respectively, so the region of a 40 mm radius is selected. When the grid independence is analyzed based on the selected computational region, the grid differs by 1.1% from 100,000 to 150,000, 2.5% from 150,000 to 180,000, 1.1% from 180,000 to 220,000, and 0.40% from 220,000 to 280,000. Therefore, the selected computational region is taken as a cylinder with a radius of 40 mm and a height of 80 mm; at the same time, the grid number is 200,000. The model material selection is the same as that in Table 1. Considering the actual situation, the levitated rotor is placed in a stainless steel thimble to constrain the range of its motion. The upper and lower symmetrical permanent magnets are placed on a soft-iron pole armature to constrain the magnetic induction lines (in the derivation of the previous equation, this structure is simplified according to assumptions i)–iii)). The magnetic field distribution is shown in Figure 5.

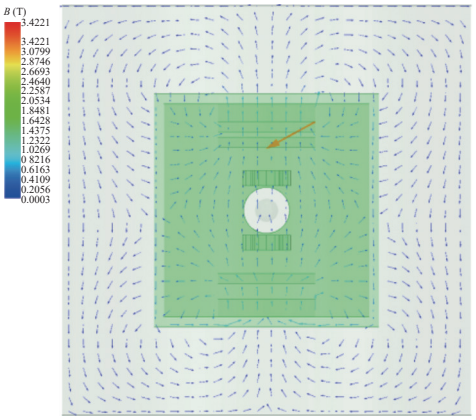

Figure 5 Magnetic field vector diagram.

To understand the influence of the electromagnetic force on the equilibrium state of the rotor, the coil is loaded with DC currents in the range of 0–0.5 A. The obtained magnetic field distribution diagram is shown in Figure 6. The positive Z-axis force on the rotor is shown in Figure 7. The strongest magnetic field occurs near the permanent magnet, and the nickel-iron alloy shell with a high permeability has a good shielding effect for the magnetic field. The force on the rotor is calculated according to the inter-

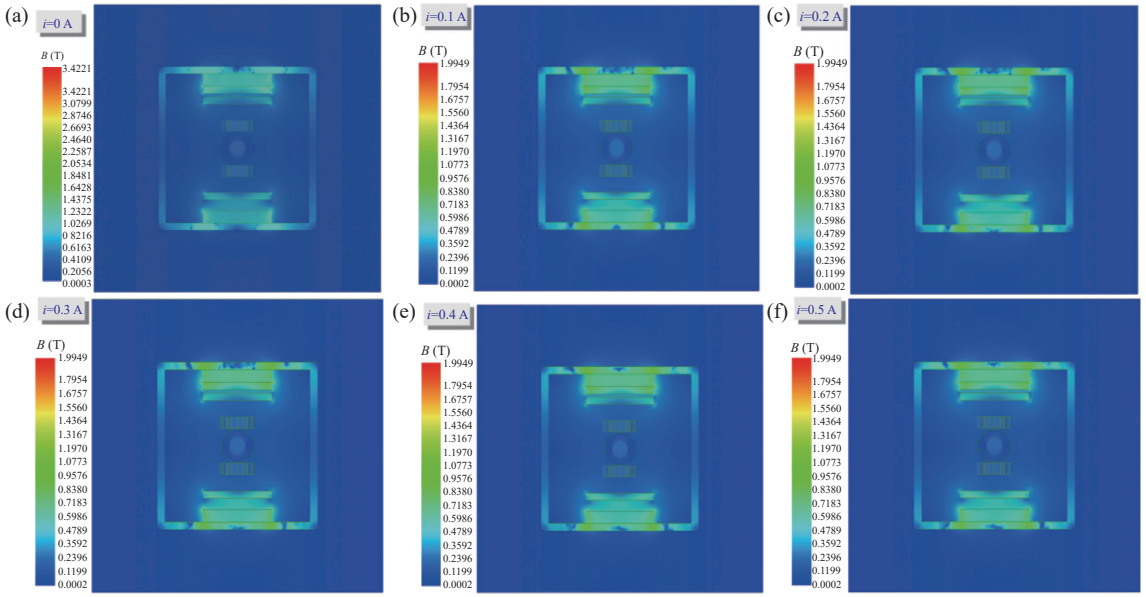

Figure 6 Diagram of the magnetic field distribution of the coil loaded with a DC current i of (a) 0 A; (b) 0.1 A; (c) 0.2 A; (d) 0.3A; (e) 0.4A; (f) 0.5A.

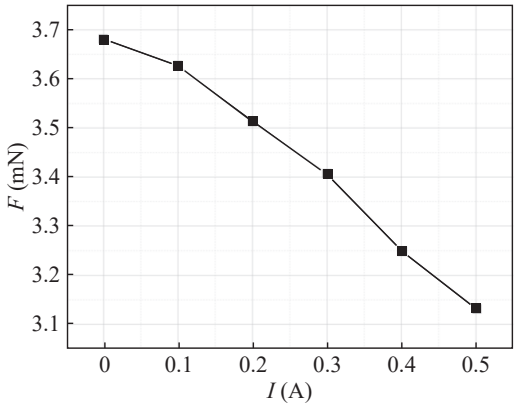

Figure 7 Relationship between the current loaded on the coil and the force on the rotor.

nal virtual displacement. The force on the rotor in the positive direction of the Z-axis is approximately 3.6812 mN, which is basically the same as its gravity (3.7216 mN). Thus, the rotor can be stably suspended in this model.

In addition, to move the rotor out of its initial position, namely, the upper or lower limit position, the forces on the rotor should be analyzed. The magnetic field distribution when the rotor is at the lower limit position is shown in Figure 8, and the electromagnetic force is shown in Figure 9. When the rotor is at the lower limit position, the forces given by the upper and lower coils are both repulsive. As the loading current increases, the rotor is subjected to an increased force in the positive direction of the Z-axis. Finally, the rotor changes from a state where it is firmly attracted by the lower permanent magnet to a state where it has a tendency to move upward. By fitting the data, the current for this change is approximately 0.36 A, with a corresponding voltage of 13.68 V. That is, if the rotor should be moved from the lower limit position to the balance point, then the loaded voltage must be greater than 13.68 V, which is basically consistent with the experimental performance.

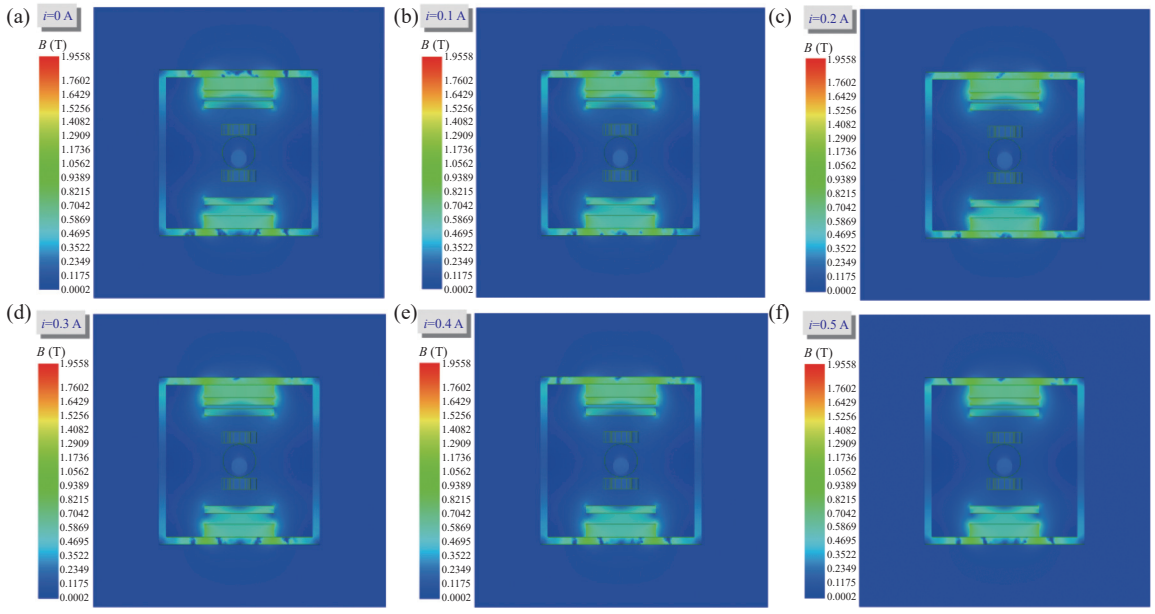

Figure 8 Diagram of the magnetic field distribution of the rotor at the lower limit position with the DC current i of (a) 0 A; (b) 0.1 A; (c) 0.2 A; (d) 0.3A; (e) 0.4A; (f) 0.5A.

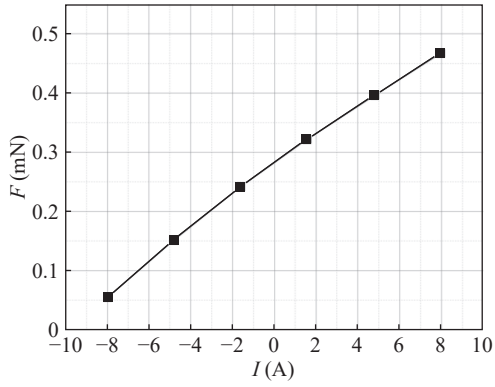

Figure 9 Relationship between the current loaded on the coil and the force on the rotor when the rotor is at the lower limit position.

Similarly, when the rotor is at the upper limit position, the corresponding voltage is approximately 12.16 V. The difference between the two voltages is mainly because the rotor needs more energy to overcome the work of gravity when it is at the lower limit position.

As mentioned above, the ultimate loading currents for the rotor at the upper and lower limit positions are 0.32 A and 0.36 A, respectively. To understand the effect of the loading current on the rotor when it is out of the initial state, a DC current of 0.4 A is applied to the coil to analyze the force and motion of the rotor at different positions. The magnetic field distribution of the rotor at different positions is shown in Figure 10, and the forces on the rotor at different positions are shown in Figure 11.

According to the calculation result, as illustrated in

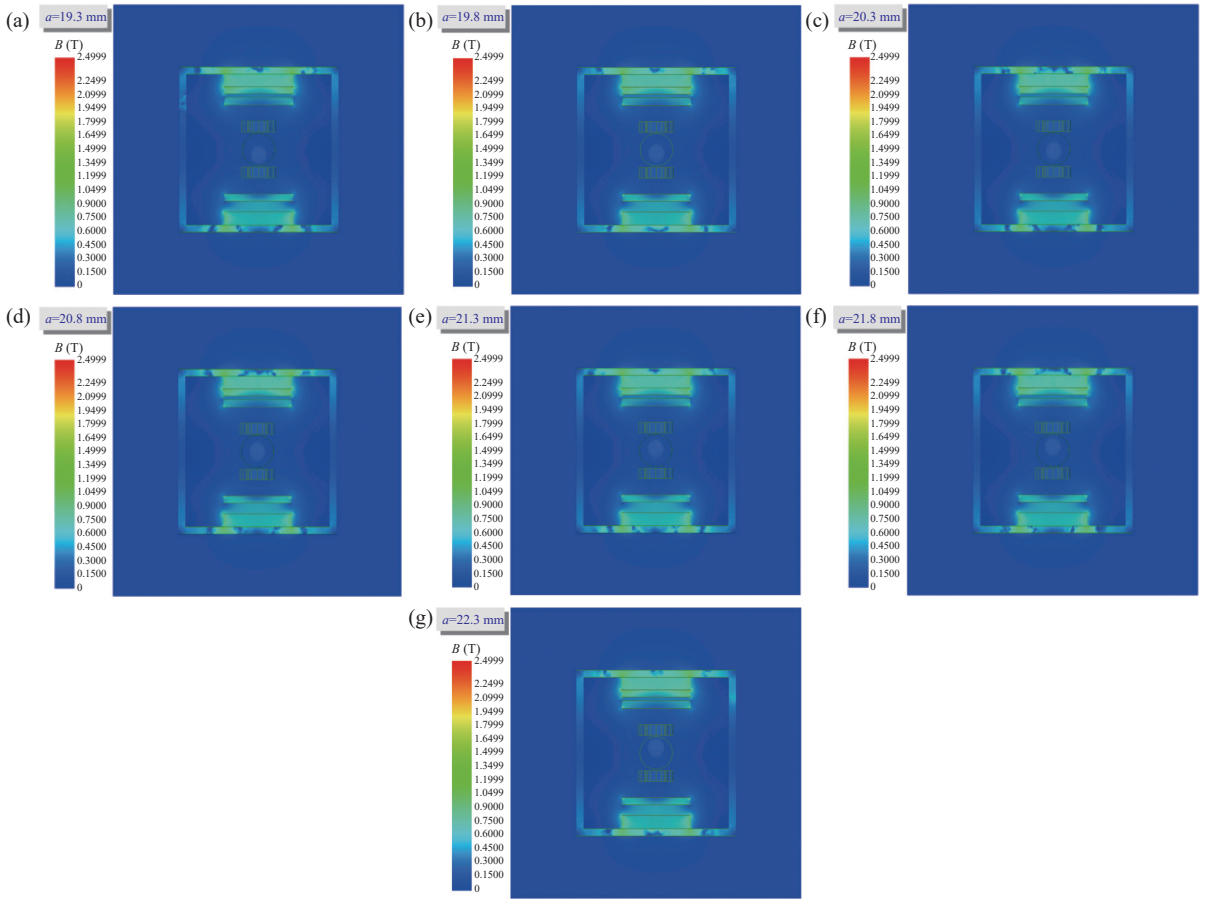

Figure 10 Diagram of the magnetic field distribution of the rotor at different positions *a* of (a) 19.3 mm; (b) 19.8 mm; (c) 20.3 mm; (d) 20.8 mm; (e) 21.3 mm; (f) 21.8 mm; (g) 22.3 mm.

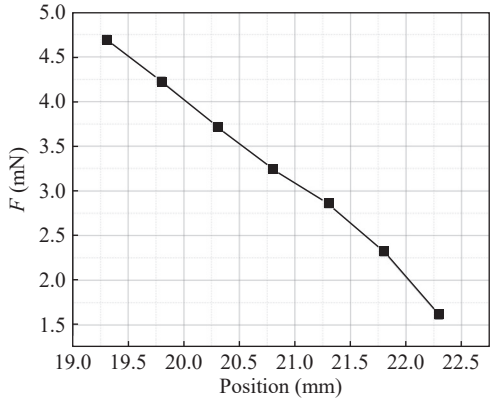

Figure 11 Force on the rotor at different positions under a 0.4 A current.

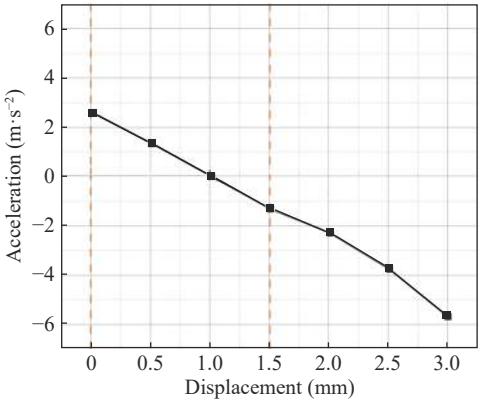

Figure 12 Relationship between rotor displacement and acceleration.

Figure 12, the initial acceleration is approximately 2.62 m/s^2. The rotor moves from downward to upward, and its displacement from the equilibrium position is 1.5×10^{-3} m. By integrating the acceleration over the displacement of 0–1.5×10^{-3} m, it is easy to obtain that the rotor velocity at the equilibrium position is approximately 5.1×10^{-2} m/s. The current of 0.4 A is too large for the rotor in this case, and its acceleration has not changed direction when it passes the equilibrium position. Through further optimization, an excitation current of 0.38 A will ensure that the rotor stops exactly near the equilibrium point.

3) Levitation experiment

Using the device shown in Figure 13(a), the coil position was adjusted by utilizing three-dimensional adjustable micrometers so that the eddy current displacement sensor operated in the optimal linear region.

To verify the correctness of the PM-EM hybrid magnetic levitation model established with the parameters designed above, the system shown in Figure 13(b) was tested. Frequency domain analysis of the levitation displacement response of the magnetic levitation control system was per-

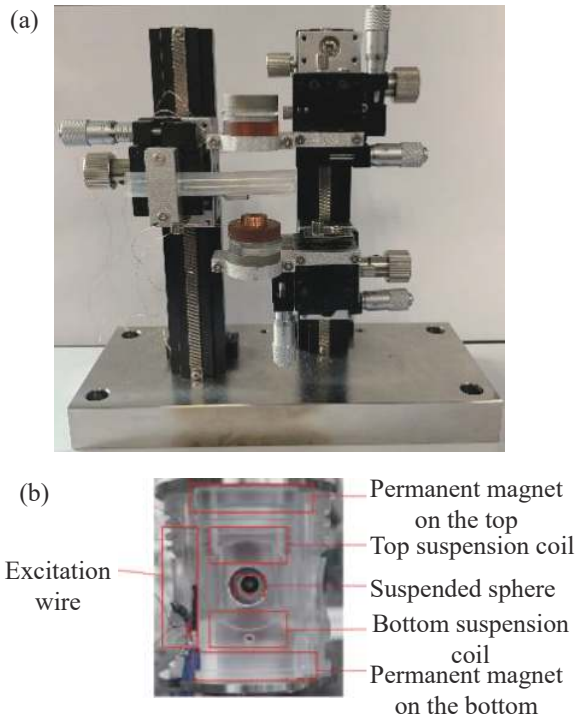

Figure 13 Diagram of the experimental setup.

formed using a frequency counter.

The levitation displacement response was recorded after adjusting the PID parameters to stabilize the levitation, as shown in Figure 14.

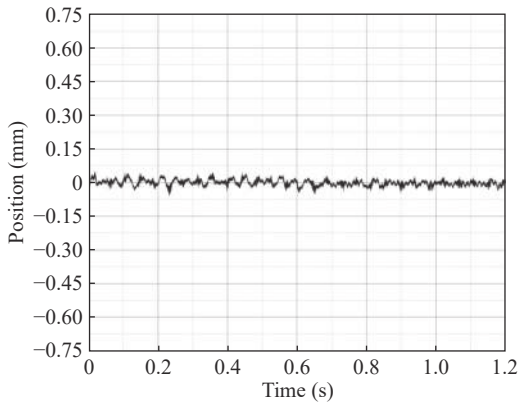

Figure 14 Displacement response over time.

As shown in Figure 14, the levitation is stable, and the amount of axial position fluctuation is within ±0.06 mm.

Using an oscilloscope to record the current loaded on the coil, as seen in Figure 15, the current is found to fluctuate within ±0.02 A when the rotor is suspended in the center. The current recording indicates that the single-degree-of-freedom permanent magnet-biased rotor suspension system accomplishes stable levitation with low power consumption.

2. High-speed rotary stepper drive system

The horizontal rotation of the rotor is achieved by loading a rotating magnetic field (see Figure 16) generated by the

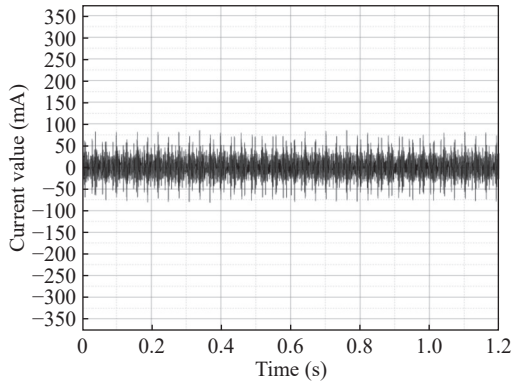

Figure 15 Suspension control current.

four self-supporting rotary drive coils around the rotor. Similar to the driving principle of a stepper motor [24], [25], as shown in Figure 17, two AC phases are fed into the driving coils A, B, C, and D (two coils are connected in series for one phase). The microprogrammed control unit (MCU) continuously outputs the pulse width modulation (PWM) and direction pulse signal to the motor driver. Due to the difference between the rotational angular frequency of the rotor and the frequency of the rotating magnetic field, eddy currents are induced inside the rotor.

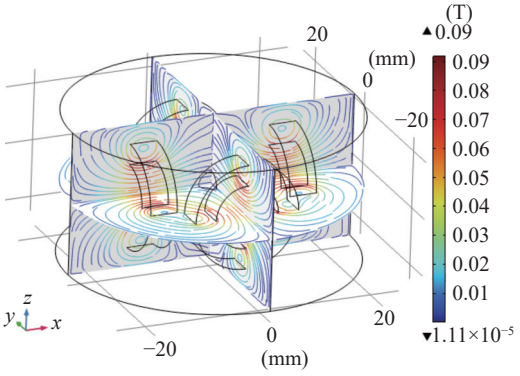

Figure 16 Diagram of the rotating magnetic field generated by the rotary drive coils.

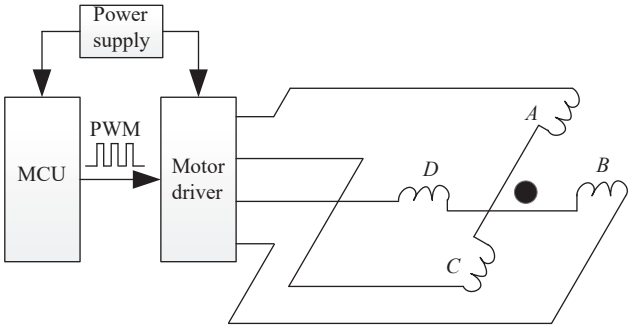

Figure 17 Schematic diagram of the stepper driver.

As shown in Figure 18, the eddy current is mainly distributed toward the surface that is directly opposite to the rotary drive coil as well as the point with the greatest skin depth. Additionally, it also reveals that when the rotor finally reaches the steady state, the average temperature of the

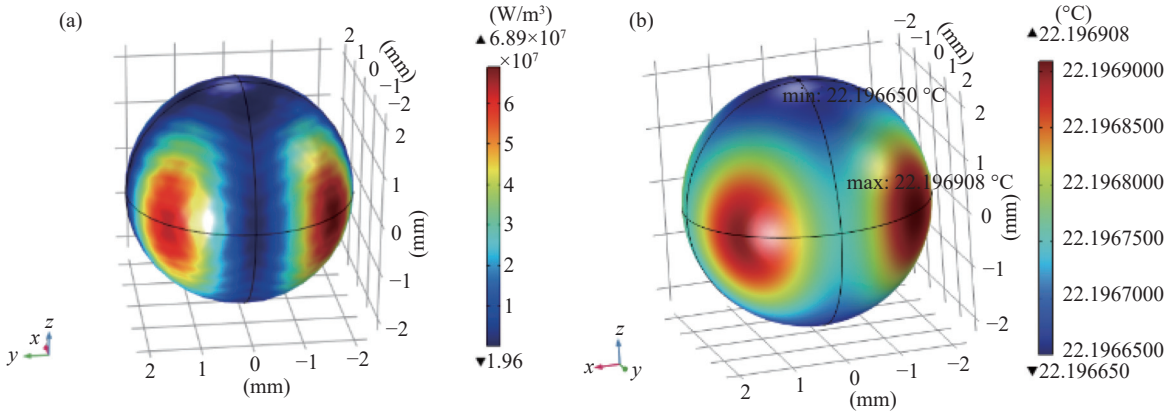

Figure 18 Distribution of (a) the eddy current and (b) temperature inside the rotor.

rotor has increased by 2.19 ℃.

The acceleration curve of the rotor generated by the drive circuit is shown in Figure 19. The average acceleration rates in the two tests are 1.66 Hz/s and 1.62 Hz/s, respectively. The differences are mainly caused by the rotor temperature increase due to the eddy currents. Since the rotating magnetic field provided by the high-speed rotary stepper drive system has a constant torque, the acceleration time for the rotor to reach a given speed increases as the temperature increases, namely, the acceleration rate decreases.

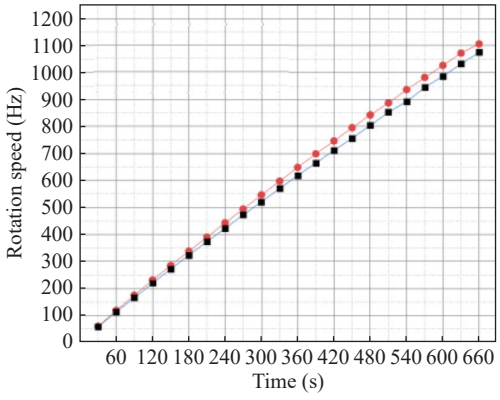

Figure 19 Rotational angular velocity vs. time.

3. Rotational angular velocity determination system

As shown in Figure 20, two signal induction (pickup) coils can sense the rotating magnetic moment of the spherical rotor in the thimble. Accordingly, the induced electric potential can be obtained as

$$E(t) = -\frac{\mathrm{d}\Phi_B}{\mathrm{d}t} = -N \cdot S \cos\theta \frac{\mathrm{d}B(t)}{\mathrm{d}t} \tag{18}$$

where Φ_B is the magnetic flux, N is the number of turns of the induction coil, S is the cross-sectional area of the pickup coil, and θ is the angle between the normal direction of the coil plane and the direction of the magnetic field.

However, the raw signal is only tens or hundreds of μV; at the same time, the high-frequency excitation signal and

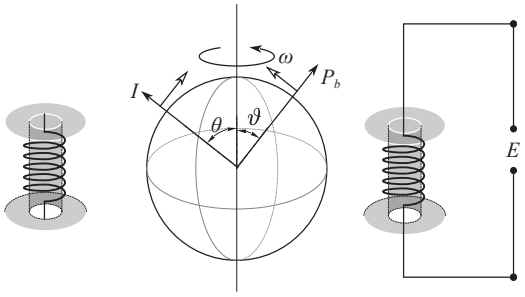

Figure 20 Diagram of the determination of the rotational angular velocity.

rotational drive signal are strong background noise. Therefore, an INA103 high-precision instrument amplifier is used to amplify the weak signal. In this design, the amplification is set to 2000 times, and the amplified signal is filtered and shaped by a low-pass filter and a comparison circuit to obtain a TTL square wave pulse signal with the same frequency as the rotational angular velocity. In addition, the signal amplitude is related to the rotational angular velocity. As shown in Figure 21, the experiment shows that the signal amplitude is the largest in the rotational angular velocity range of 400 Hz to 450 Hz. When the rotor rotates, the magnetic polarization axis has an angle with the rotational axis (see Figure 20). With rotational speed changes, the angle changes accordingly, so the magnetic flux in the pickup

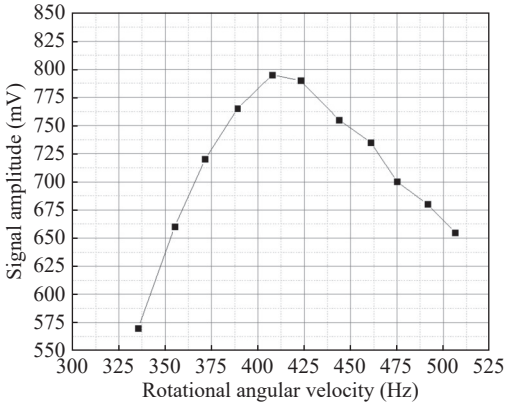

Figure 21 Curve of the signal vs. rotational angular velocity.

coil changes, and then, the signal amplitude also changes. To ensure the quality of the measurement signal, the working center frequency point is chosen to be 420 Hz.

4. Lateral damping system

During operation, the SRG is inevitably subject to vibration and shock from the surrounding environment, such as doors opening and closing and the low-frequency vibration of machines. Due to the self-restraint of the magnetic field in the vertical direction, the rotor will naturally recover to a steady state. However, the duration for this recovery ranges from several minutes to several hours.

As shown in Figure 22, the lateral oscillations of the rotor caused by vibration or shock could be damped by four coils distributed orthogonally. Among them, A and C are used for detection, and C and D are used to apply a force to the rotor. When the rotor vibrates laterally around the center position, an alternating voltage signal is induced in A or C. The control circuit amplifies, filters, and power amplifies the alternating voltage signal and loads it onto C or D to generate the corresponding alternating force current. After experimental testing, the results implied that the addition of the lateral damping system reduces the recovery time to less than 3 seconds.

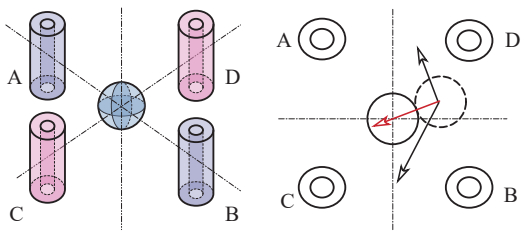

Figure 22 Schematic diagram of the lateral damping system.

IV. Metrological Characteristics

The pressure corresponding to the obtained residual drag is shown in Figure 23. The experimental results show that the changes are less than 0.49% after 50 minutes of start-up.

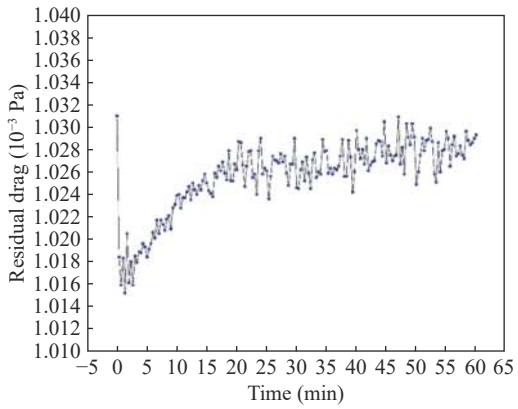

Figure 23 Pressure corresponding to the residual drag vs. time.

The SRG was calibrated against a standard gauge (SRG-2, MKS Inc.), and the calibration curve is shown in Figure 24. It can be seen that the two have good consistency and linearity, with deviations from −0.09% to + 0.368% in the range of 9.1727×10^{-5} Pa to 1.2081 Pa.

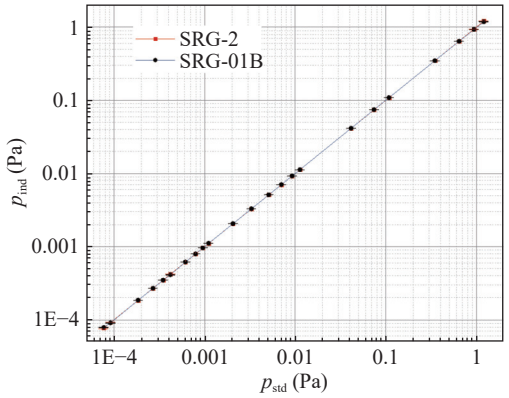

Figure 24 Calibration curve of SRG-01B(LIP) vs. SRG-2(MKS).

V. Conclusion

A metrological-grade spinning rotor vacuum gauge has been developed, and its performance has been evaluated. With the single-degree-of-freedom permanent magnet-biased rotor suspension system, the rotor is more stable. The axial position fluctuation is within ±0.06 mm. The average acceleration rate in rotor tests is 1.66 Hz/s. For the quality of the measurement signal, the working center frequency point is chosen to be 420 Hz. The change in the residual drag is less than 0.49% after 50 minutes of start-up. And finally, there is good consistency and linearity in the range of 9.1727×10^{-5} Pa to 1.2081 Pa. Subsequently, this gauge could be used for international comparison of vacuum standards and construction of national vacuum measurement traceability and transmission systems. In addition, the accuracy of the rotational angular velocity determination is mainly influenced by the quality of the levitation. Technologies such as diamagnetic levitation, superconducting levitation and optical pressure levitation are expected to further improve the levitation quality and reduce the measurement uncertainty introduced by rotor oscillation and temperature fluctuations. By carrying out research on rotational angular velocity determination systems based on photoelectric sensors and visual geometry methods, the accuracy of SRGs can be further improved.

Acknowledgement

This work was supported by the National Natural Science Foundation of China (Grant No. 61971209) and the Natural Science Foundation of Gansu Province (Grant No. 21JR7 RA742).

References

[1] K. Jousten, *Handbook of Vacuum Technology*, 2nd ed. , Wiley, Weinheim, Germany, 2016.

[2] D. T. Li, *New Technology of Vacuum Metrology*. China Machine Press, Beijing, China, 2013. (in Chinese)

[3] I. Bello, *Vacuum and Ultravacuum: Physics and Technology*. CRC Press, Boca Raton, FL, USA, 2018.
[4] G. Schweitzer and E. H. Maslen, *Magnetic Bearings: Theory, Design, and Application to Rotating Machinery*. Springer, Berlin, Heidelberg, Germany, 2009.
[5] F. T. Holmes, "Axial magnetic suspensions," *Review of Scientific Instruments*, vol. 8, no. 11, pp. 444–447, 1937.
[6] J. W. Beams, J. L. Young III, and J. W. Moore, "The production of high centrifugal fields," *Journal of Applied Physics*, vol. 17, no. 11, pp. 886–890, 1946.
[7] J. W. Beams, D. M. Jr. Spitzer, and J. P. Jr. Wade, "Spinning rotor pressure gauge," *Review of Scientific Instruments*, vol. 33, no. 2, pp. 151–155, 1962.
[8] J. C. Keith, "Magnetic torques and coriolis effects on a magnetically suspended rotating sphere," *Journal of Research of the National Bureau of Standards-D. Radio Propagation*, vol. 67D, no. 5, pp. 533–538, 1963.
[9] J. D. Nixon and D. J. Kenney, "Method for determination of magnetic moment in small spinning rotors," *Review of Scientific Instruments*, vol. 35, no. 10, pp. 1365–1366, 1964.
[10] J. K. Fremerey, "High vacuum gas friction manometer," *Journal of Vacuum Science and Technology*, vol. 9, no. 1, pp. 108–111, 1972.
[11] J. K. Fremerey, "Spinning rotor vacuum gauges," *Vacuum*, vol. 32, no. 10–11, pp. 685–690, 1982.
[12] J. K. Fremerey, "The spinning rotor gauge," *Journal of Vacuum Science & Technology A*, vol. 3, no. 3, pp. 1715–1720, 1985.
[13] G. Messer, P. Röhl, G. Grosse, *et al*., "High vacuum measured by the spinning rotor gauge: Status report of the Bureau International des Poids et Mesures intercomparison," *Journal of Vacuum Science & Technology A*, vol. 5, no. 4, pp. 2440–2443, 1987.
[14] K. Jousten, A. R. Filippelli, C. R. Tilford, *et al*., "Comparison of the standards for high and ultrahigh vacuum at three national standards laboratories," *Journal of Vacuum Science & Technology A*, vol. 15, no. 4, pp. 2395–2406, 1997.
[15] J. A. Fedchak, K. Arai, K. Jousten, *et al*., "Recommended practices for the use of spinning rotor gauges in inter-laboratory comparisons," *Measurement*, vol. 66, pp. 176–183, 2015.
[16] D. T. Li and D. X. Tian, "Metrological properties of spinning rotor gauge," *Vacuum Science and Technology (China)*, vol. 19, no. S1, pp. 15–18, 1999. (in Chinese)
[17] D. T. Li, "Study on transfer coefficient of spinning rotor gauge," *Vacuum & Cryogenics*, vol. 11, no. 3, pp. 139–143,186, 2005. (in Chinese)
[18] ISO 24477: 2022, Vacuum Technology-Vacuum Gauges-Specifications, Calibration and Measurement Uncertainties for Spinning Rotor Gauges, Available at: *https://www.iso.org/standard/78872.html*.
[19] J. K. Fremerey, "Apparatus for determination of residual drag torque on small spinning spheres in magnetic suspension," *Review of Scientific Instruments*, vol. 42, no. 6, pp. 753–762, 1971.
[20] H. Isogai, "An analysis of the effects of eddy currents on the accuracy of a Spinning Rotor Gauge," *Vacuum*, vol. 48, no. 2, pp. 175–179, 1997.
[21] H. Isogai, "An analysis on total offset pressure of spinning rotor gauge," *IEEJ Transactions on Fundamentals and Materials*, vol. 117, no. 12, pp. 1177–1181, 1997.
[22] J. K. Fremerey, "Significant deviation of rotational decay from theory at a reliability in the 10^{-12} sec^{-1} range," *Physical Review Letters*, vol. 30, no. 16, pp. 753–757, 1973.
[23] S. R. Cong, Y. L. Wang, and Y. L. Zhang, "Model CXG-1 magnetic suspension spinning rotor vacuum gauge," *Chinese Journal of Scientific Instrument*, vol. 6, no. 1, pp. 41–50, 1985. (in Chinese)
[24] P. G. D. de Almeida, "Cylindrical spinning rotor gauge-A new approach for vacuum measurement," *Master Thesis*, University of Lisbon, Alameda da Universidade, Cidade Universitária, Lisboa, 2015.
[25] M. Schuck, T. Nussbaumer, and J. W. Kolar, "Characterization of electromagnetic rotor material properties and their impact on an ultra-high speed spinning ball motor," *IEEE Transactions on Magnetics*, vol. 52, no. 7, article no. 8204404, 2016.

Detian Li was born in Gansu Province, China. He received the Ph.D. degree in physical electronics from China Academy of Space Technology in 2007. He is an Academician of the Chinese Academy of Engineering and the International Academy of Astronautics. His research interests include vacuum measurement technology and multiple parameters tests in vacuum environment.
(Email: lidetian@hotmail.com)

Meiru Guo was born in Gansu Province, China. He received the Ph.D. degree in physical electronics from China Academy of Space Technology in 2010. He is now a Professor of Lanzhou Institute of Physics. His research interests include vacuum metrology technology and vacuum measurement instrument development.
(Email: meiruguo@163.com)

Zhenhua Xi was born in Gansu Province, China. He received the Ph.D. degree in physical electronics from China Academy of Space Technology in 2019. He is now a Senior Engineer of Lanzhou Institute of Physics. His research interests include vacuum metrology technology and vacuum measurement instrument development.
(Email: comanche_xzh@126.com)

Huzhong Zhang was born in Gansu Province, China. He received the Ph.D. degree in physical electronics from China Academy of Space Technology in 2020. He is now a Senior Engineer of Lanzhou Institute of Physics. His research interests include vacuum metrology technology and vacuum measurement instrument development.
(Email: comanchejanehuge@126.com)

Bowen Li was born in Gansu Province, China. He received the B.S. degree in electronics science and technology from Nankai University. He is now a postgraduate student of Lanzhou Institute of Physics. His research interests include vacuum metrology technology and vacuum measurement instrument development.
(Email: bwenlee@163.com)